Available online at www.sciencedirect.com
ScienceDirect
Computers & Fluids 37 (2008) 857–866
computers & fluids
www.elsevier.com/locate/compfluid

# Near stall simulation of the flow around an airfoil using zonal RANS/LES coupling method

F. Richez [a,*], I. Mary [a], V. Gleize [a], C. Basdevant [b]

[a] ONERA, Computational Fluid Dynamics and Aeroacoustics Department, BP 72 - 29, Avenue de la Division Leclec, 92322 Chatillon, France
[b] Ecole Normale Superieure/LMD, 24 rue Lhomond – 75231 Paris cedex 05, France

Received 1 October 2006; received in revised form 22 December 2006; accepted 16 March 2007
Available online 29 September 2007

**Abstract**

The objective of this current study is to investigate the course of events leading to stall just before its occurrence. The stall mechanisms are very sensitive to the transition that the boundary layer undergoes near the leading edge of the profile by a Laminar Separation Bubble (LSB). To provide helpful insights into this complex flow, different LES of the flow around an airfoil near stall have been achieved. Attention has been given to the transition mechanism in the LSB. In particular, the results are successfully compared to the linear stability theory. Furthermore, a zonal Reynolds averaged Navier–Stokes/large eddy simulation (RANS/LES) hybrid method has been employed for the same flow configuration to resolve more accurately the transitional flow than with the RANS approach. The analysis of the results highlights the strong impact of the LSB structure on the downstream boundary layer.


## 1. Introduction

Thanks to the Reynolds Averaged Navier–Stokes (RANS) approach, the calculation of flows around a whole aircraft is nowadays possible. However, many studies seem to prove that this approach is not mature for the prediction of complex flow phenomena: for example, the numerical simulation of the flow around an airfoil at static and dynamic stall is still a very challenging task for CFD application.

The dynamic stall flow phenomenon concerns the delay in the stalling characteristics of airfoils, rapidly pitched beyond the static angle. The dynamic stall has serious implications in terms of achievable performance, which needs to be predicted accurately as soon as possible in the airfoil design cycle. The account of this phenomenon is important for the design of many industrial domains, such as helicopter rotor blades (retreating blade) or jet engines (rotating stall). It is characterized by a massive unsteady flow separation and by the formation of large scale vortical structures at the origin of hysteresis effects. As a result, the maximum values of lift and pitching moment highly exceed their static values.

Hence, because of manufacturing interest, the unsteady RANS (URANS) equation simulation has been widely used to compute dynamic stall flow. Unfortunately, the results are far from being totally reliable for predicting the dynamic stall behavior of airfoils [1] and have a large computational cost. In this context, some researchers have chosen to start from scratch by considering static stall. They have proved that the solution is very sensitive to the grid resolution and to the turbulence model [2]. Even, when in the more simple case of static stall, the RANS simulation does not predict correctly the stall occurrence.

The flow over an airfoil near maximum lift combines different complex mechanisms which still challenge RANS methods. Indeed, the transition of the boundary layer usually happens close to the leading edge by a LSB. Next, the turbulent boundary layer remains attached on the middle area of the airfoil profile before separating near the trailing edge. Thereby, the massive flow separation of stall may result from the increase of the turbulent separation area or the breakdown of the LSB. Otherwise, the interaction

* Corresponding author. Tel.: +33 1 46 73 4040; fax: +33 1 46 73 4141.
*E-mail address:* Francois.Richez@onera.fr (F. Richez).

0045-7930/$ - see front matter © 2007 Elsevier Ltd. All rights reserved.
doi:10.1016/j.compfluid.2007.03.016

between these laminar and turbulent separations should have to be considered to understand the stall mechanism. In all the cases, this phenomenon is very sensitive to the transition of the boundary layer. This may be one of the reasons why the RANS approach, which is not designed for simulating transition, fails to predict stall occurrence. Since large eddy simulation (LES) provides an effective tool for tackling such flow conditions, we have decided, in this study, to use a zonal RANS/LES coupling method [3,4] to combine the advantages of the two approaches: LES for the transitional flow, and RANS for the attached and separated fully turbulent boundary layer.

First, two zonal RANS/LES coupling simulations have been performed, with the same flow configuration, a LES domain been located in the whole suction side of the boundary layer and in the wake zone, but with two different grid resolutions. These simulations can almost be considered as full LES and will be called LES thereafter. The results are compared and discussed in this manuscript. In particular, we give a detailed account of the numerically observed transition. In the finest grid case, the disturbances that appear, grow and lead to the transition in the LSB are successfully compared to a linear stability analysis. Finally, we have performed a RANS/LES coupling simulation with a much smaller LES domain located in the transitional zone. The results of this simulation, called RANS/LES thereafter, are compared to the LES and full RANS simulation, and the improvement of the solution emphasized.

## 2. Numerical method

The compressible Navier–Stokes equations are solved in a multibloc structured solver based on a finite volume method. Overlapping RANS and LES domains are used (see Fig. 1). In the RANS domain, the Spalart–Allmaras model is used to take into account the pressure side turbulent boundary layer. In the LES domain, the selective mixed scale model is used to model the subgrid scale terms [5]. At each time step, the values of the conservative variables in the RANS domain of the overlapping zone are computed by averaging the LES variables in the cell volume of the RANS domain. Moreover, these conservative variables are used to transport the turbulent viscosity of the Spalart–Allmaras model. The information transfer between the RANS domain and the LES one requires some boundary conditions. They are obtained by the use of ghost cells and enrichment procedure [6].

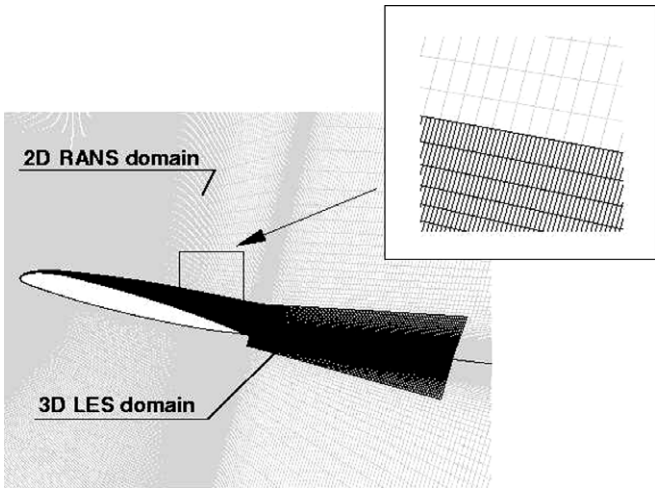


Fig. 1. LES mesh.

The viscous fluxes are discretized by a second-order accurate centered scheme. For the Euler fluxes discretization, a hybrid centered/upwind version of the AUSM+(P) scheme, whose dissipation is proportional to the local fluid velocity, is employed [7]. For efficiency reason, an implicit time integration is employed to deal with the very small grid size encountered near the wall. Then a three-level backward differentiation formula is used to approximate the temporal derivate, leading to a second-order accuracy. An approximate Newton method is used to solve the nonlinear problem. At each iteration of the inner process, the resolution of the linear system relies on the Lower–Upper Symmetric Gauss–Seidel (LU-SGS) implicit method. These numerical methods, developed at the ONERA in the FLU3M code, have been validated in several applied computations [7–9].

## 3. Flow and computation parameters

The OA209 profile, which is an helicopter fan blade profile, has been retained for this study. The Reynolds number, based on the chord and the freestream velocity, is 1.8 million and the freestream Mach number is equal to 0.16. The angle of attack is 15 degrees which is, according to experimental studies achieved by the ONERA [10], just prior the stall occurrence.

The LES domain is located in the whole suction side of the boundary layer and in a region of one chord length in the wake zone (see Fig. 1). Compared to the RANS domain, the LES grid is much refined in the streamwise direction and keeps the same resolution in the wall normal direction. To reduce the computational cost, the LES domain is decomposed into several sub-domains, which differ by their spanwise extent and spanwise resolution. The spanwise extent has been chosen to be greater than the boundary layer thickness along the profile [6]. At the interface between these domains, the shorter domain in the spanwise direction imposes the flow periodicity, since its information is duplicated in the ghostcells of the larger domain.

For both grids, the mesh resolution usually required by LES for wall bounded flow is reached everywhere [11,12,9]. The first mesh M1 satisfies, all along the suction side of the boundary layer, the following conditions expressed in wall unit: $\Delta x^+ \leqslant 70, \Delta y^+ \leqslant 2$ and $\Delta z^+ \leqslant 15$, where $x$, $y$ and $z$ denote respectively the streamwise, wall normal and spanwise directions. The second mesh used, called M2, is refined in the streamwise direction to satisfy $\Delta x^+ \leqslant 50$, while the

Table 1
Calculation and mesh parameters of the two LES

| | $\Delta t$ (s) | CPU (h) | $N_{pts}$ (RANS) | $N_{pts}$ (LES) |
|---|---|---|---|---|
| LES M1 | $1.5\times10^{-7}$ | 4000 | $1153\times101$ | $9.9\times10^{6}$ |
| LES M2 | $1.3\times10^{-7}$ | 5000 | $1259\times101$ | $12\times10^{6}$ |

grid resolution in the other directions does not change. Therefore, for both grids, the resolution is sufficient to resolve accurately the streaks of a turbulent boundary layer, while the smaller structures, assumed as isotropic, are modeled by the subgrid scale term. However, no criteria exists for the grid resolution in a transitional separated bubble. The M2 grid has been hence strongly refined (almost four times in the streamwise direction) in the transitional zone, near the leading edge, so that the mesh resolution tends to a DNS one in this area. Thereby, the influence of the grid refinement in the LSB should have a predominant effect on the results. The other numerical parameters are summed up in Table 1.

The code is parallelized using a domain decomposition technique based on the openMP directive. The computation has been running at 13 Gflops on four processors NEC SX5 during several thousands of total CPU hours to ensure that the unsteady solution fluctuates around a stationary averaged state. The statistical variables presented thereafter have been computed during the last five periods of the vortex shedding occurring at the trailing edge.

## 4. Aerodynamics results

The results obtained with the M1 and M2 meshes have been compared to experimental data [10] and to a fully turbulent RANS simulation using Spalart–Allmaras (SA) model. This RANS simulation has been computed on the RANS domain used for M2. Furthermore, the same modified AUSM+(P) scheme has been employed to show the effects of the turbulence modeling when comparing the results. Then, the LES lift and drag values are compared to the experimental and the RANS ones in Table 2. The M1 solution is closer to experimental data and the grid refinement leads to a decrease of the lift and an increase of the drag. The RANS simulation strongly over-estimates the lift coefficient. The temporal evolution of the lift and drag coefficients (not presented here) shows, for both LES, some oscillations, due to a vortex shedding at the trailing edge. The frequency of this phenomenon corresponds to a Strouhal number of $S_t \approx 0.2$ as expected. During the last five periods of the vortex shedding, the lift seems to oscillate around a constant value, insuring the solution is statistically converged.

Table 2
Experimental and numerical lift and drag coefficients

| | Experiment | LES M1 | LES M2 | RANS SA |
|---|---|---|---|---|
| Lift | 1.416 | 1.450 | 1.366 | 1.487 |
| Drag | 0.029 | 0.030 | 0.039 | 0.023 |

We can see a general good agreement, in Fig. 2a, between experimental, LES and RANS pressure distributions ($C_p$). With both M1 and M2 grids, LES provides a flattened shape of the $C_p$ distribution at the leading edge (see Fig. 2c), which is characteristic of a separated flow. One can notice that no such shape is observed for the fully turbulent RANS simulation because of the premature increase of the turbulence viscosity. Comparing M1 and M2, the grid refinement in this region leads to an increase of the LSB length. Unfortunately, the streamwise resolution of the experimental measurements is not sufficient to draw a conclusion concerning the location and the size of the LSB. However, the size of a LSB is very sensitive to the freestream turbulence intensity and to the surface roughness [13,14]. It seems likely that the LSB size will be different between experiment and LES, until these effects are not considered. For all that, this complex issue is not discussed here.

The larger LSB length, observed with M2, is accompanied by strong changes of the mean pressure value $C_p$ and of the mean streamwise compression $dC_p/dx$, downstream the reattachment point (see Fig. 2c and d). The stiff drop of $C_p$, between 1% and 1.4% of chord, is apparently due to the grid refinement in this region. Indeed, with the finer grid, the vortices structures in this transitional area are better-resolved. As a consequence, the mechanism of energy transfer from the freestream flow to the turbulent boundary layer is reinforced, which leads to larger turbulence intensities (see Fig. 5), and a stronger drop of the boundary layer edge velocity.

As can be seen in Fig. 2b, the change of the LSB structure between the two LES grids has an important effect on the turbulent separation that occurs at the trailing edge. The coarser LES, like the RANS simulation, under estimates the experimental $C_p$ value, whereas the finer LES over estimates its value. The larger turbulent separation at the trailing edge, we can observe with M2, modifies the circulation around the airfoil, which leads to a decrease of the velocity pick at the leading edge. This lower $C_p$ pick value is closer to the first experimental $C_p$ value than the one obtained with M1 (see Fig. 2c).

Looking at Figs. 3 and 4, we can first observe the discrepancy of the boundary layer thickness between the two LES, at 2% of chord. Although almost identical to M1 at the separation point where the flow is laminar, the boundary layer thickness becomes larger, for M2, at the reattachment point (see Fig. 5). Indeed, with the finer grid, the instability growth mechanism in the separated shear layer can occur (as it will be seen in Section 4), whereas, with M1 grid, the subgrid viscosity prevents a realistic growth of these instabilities. As a consequence, the flow reattaches upstream with M1, and the boundary layer thickness, at the reattachment point, is smaller. Then, this discrepancy of the boundary layer thickness is convected downstream.

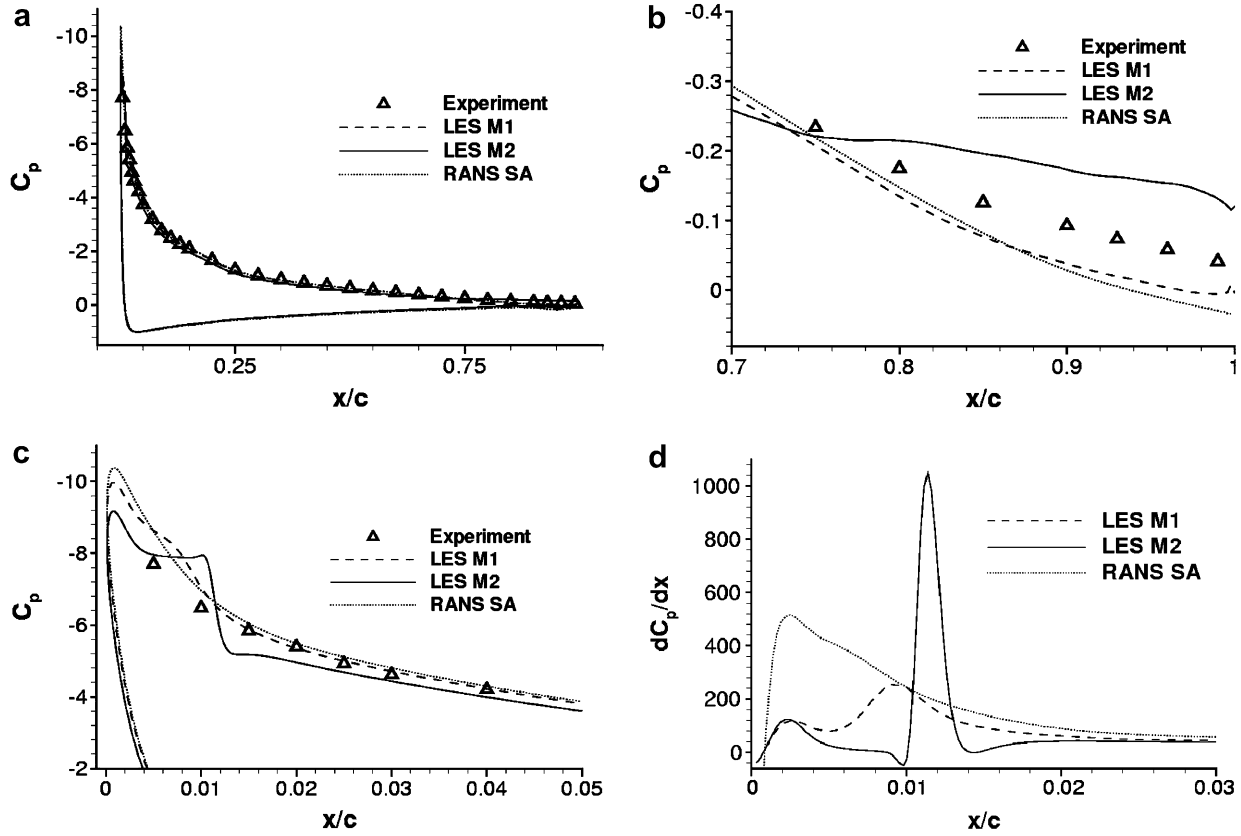


Fig. 2. $C_p$ distribution on the whole airfoil profile (a), at the trailing edge (b), and at the leading edge (c) and streamwise variation $dC_p/d(x/c)$ at the leading edge (d).

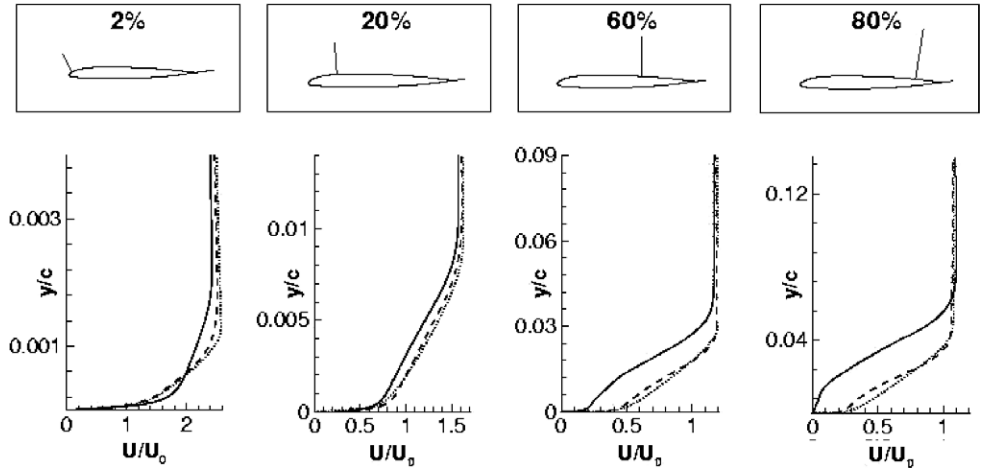


Fig. 3. Mean velocity profiles at different locations on the suction side of the airfoil: ---, LES M1; —, LES M2; ···, RANS SA M2.

Another important remark concerns the adverse pressure gradient (APG) characteristics. Except in the LSB region and near the trailing edge, the APG strength is almost identical between RANS and LES, on the bulk airfoil surface. However, we can observe, in Fig. 3, the lack of ability of the RANS method to capture the APG effects on the mean velocity profiles. The behaviors of different turbulence models, in an idealised turbulent APG boundary layer, have recently been tested [15], and a detailed analysis of the turbulence kinetic energy budgets have indeed enlightened the weaknesses of each model. Looking at the LES results, we can observe typical shapes of the velocity fluctuations and of the turbulent Reynolds shear stresses (see Fig. 4), characteristics of APG [16,17]. The turbulence intensities, in both cases, are reduced in the near-wall region and increased in the outer layer. However, the outer-layer turbulence becomes more energetic with M2 grid. It may be a consequence of the change of the $C_p$ dis-

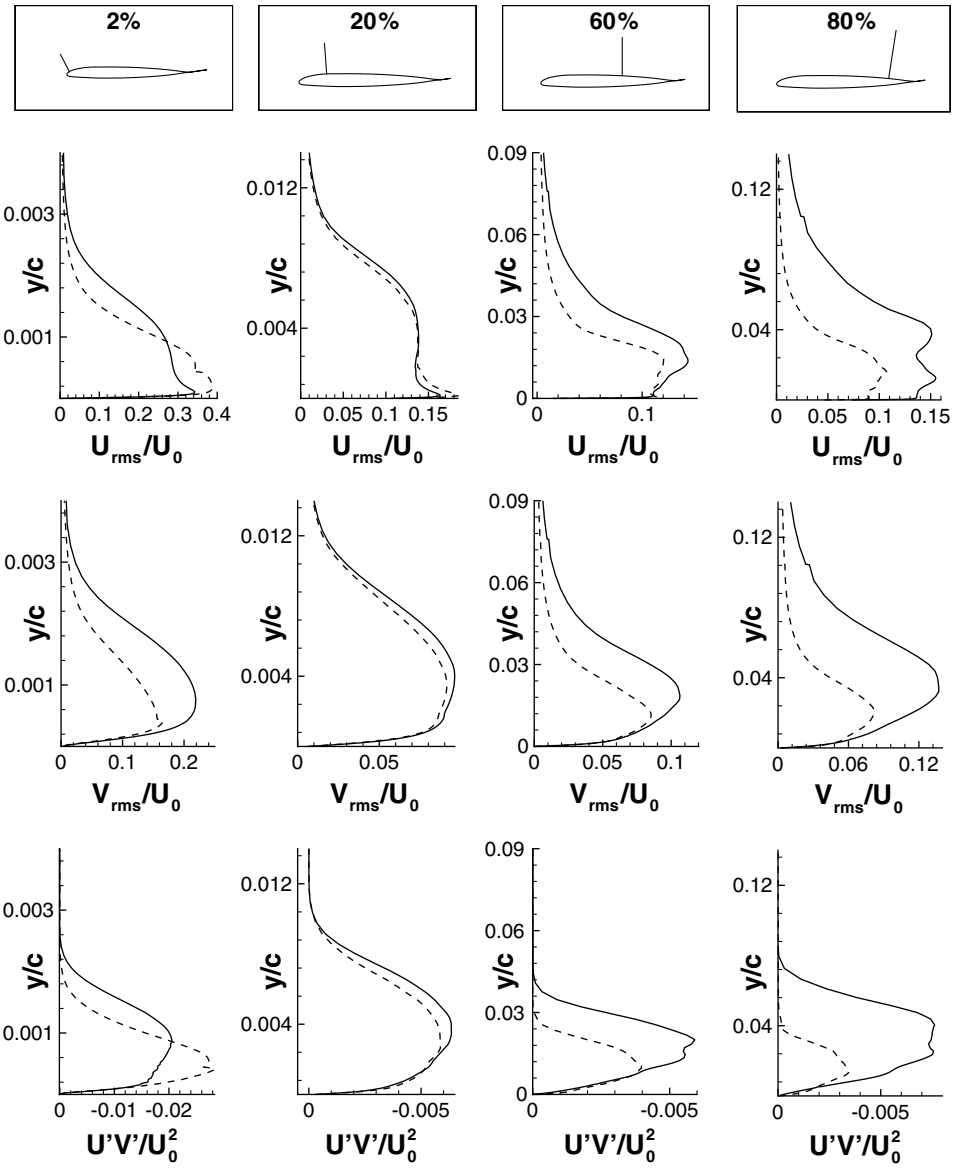


Fig. 4. Rms velocity profiles ($U_{rms}/U_0$, $V_{rms}/U_0$ and $U'V'/U_0^2$) at different locations of the suction side of the airfoil: ---, LES M1; —, LES M2.

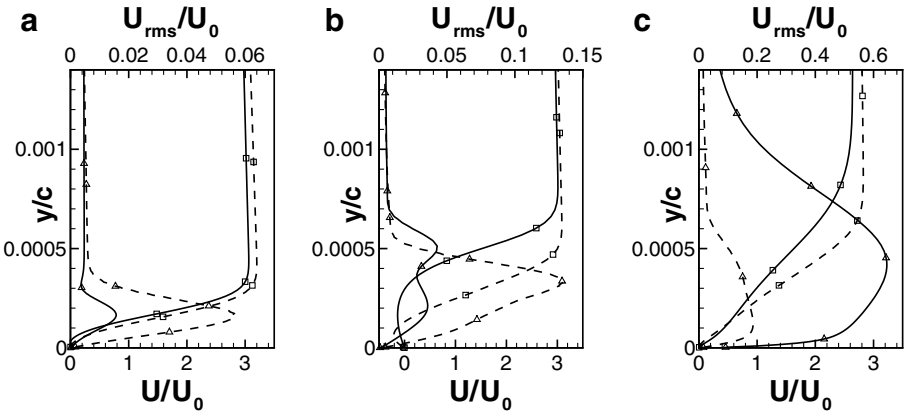


Fig. 5. Mean velocity and streamwise velocity fluctuation profiles in the LSB: □, $U/U_0$; △, $U_{rms}/U_0$; ---, LES M1; —, LES M2; (a) at the separation point; (b) at 50% of LSB length; (c) at the reattachment point.

tribution. Indeed, it has been shown that the mean streamwise compression $dC_p/dx$ can directly influence the way the outer-layer turbulence increases [18,17]. Since the larger LSB of M2 induces a strong effect on the streamwise variation of $C_p$ (see Fig. 2d), it may explain the differing variations of the outer-layer turbulence intensities, between M1 and M2.

Hence, it seems that the change of the LSB structure between the two LESs has a deep impact on both the boundary layer thickness and the way the outer-layer turbulence intensity increases. These two effects explain why the turbulent boundary layers of M1 and M2 grids do not have the same history, and therefore the same behavior near the trailing edge where it separates at 80% of chord for M2 and it does not for M1.

## 5. Analysis of the transition

The important discrepancy between these two LESs emphasizes the crucial effect of the LSB structure on the whole rearward flow. Therefore, we have decided to carry out a more detailed analysis of the flow in the transitional zone for these two simulations. Following, the instability mechanism numerically observed for the finer grid is compared to a local linear stability analysis.

### 5.1. Statistical results

For both M1 and M2 grids, the laminar boundary layer separates at 0.4% of chord from the leading edge. Despite the grid refinement, the laminar boundary layer thickness, at the separation point, is almost identical between the two meshes (see Table 3 and Fig. 5a). Hence, the grid refinement does not change the boundary layer thickness upstream the separation point. The edge velocity at the separation point is obviously slightly different since the differing turbulent separation near the trailing edge changes the circulation around the airfoil profile. It is then expected that the instability mechanism which the boundary layer undergoes in the LSB should be almost identical. We can though observe that the mean velocity profiles and the velocity fluctuations profiles, shown in Fig. 5b, are strongly different. The growth rate of the unstable waves is also hugely different between the two grids. The fluctuations observed with the M1 mesh grow almost linearly, which is meaningless according to the linear stability theory [19]. The fluctuations are apparently quickly dissipated because of the low grid point density in this area (see Table 3). Then, the instability mechanism cannot occur in a realistic manner with the M1 grid. This leads to a smaller LSB length, a smaller boundary layer thickness at the reattachment point (see Table 3), and smaller turbulence intensities at the reattachment point (see Fig. 5c). On the other hand, the fluctuations observed with M2 seem to have an exponential growth with a strong growth rate, which is more realistic. The ensuing maximum fluctuations at the reattachment point are larger. The $u_{rms}$ attains 60% of the free-stream velocity, which represents 23% of the boundary layer edge velocity and is close to the value found by Yang and Voke in their flat plate case [20]. One can see that the shape with two peaks of $u_{rms}$ profiles in Fig. 5b looks like instability waves in a transitional separated flow already observed in DNS [21].

Table 3
$L_b$: averaged LSB length; $\delta_S/c$: boundary layer thickness at the separation point; $\delta_R/c$: boundary layer thickness at the reattachment point; Nx, Ny: number of points in the LSB in the streamwise and in the wall normal direction; Nx/$\lambda$: number of points by wavelength of the disturbances that appear in the LSB

| | $L_b/c$ | $\delta_S/c$ | $\delta_R/c$ | Nx | Ny | Nx/$\lambda$ |
|---|---|---|---|---|---|---|
| LES M1 | 0.95% | 0.04% | 0.08% | 30 | 30 | 4–5 |
| LES M2 | 1.27% | 0.04% | 0.12% | 160 | 40 | 12–23 |

### 5.2. Fourier analysis

To study more accurately the instability mechanism that the flow undergoes in the LSB, we have calculated a Fourier transform of the pressure signals obtained with the M2 mesh at different locations along the bubble. The mean velocity profile at each location in the LSB is represented in Fig. 6 and the corresponding pressure spectrum in Fig. 7a. The spectrum amplitude level increases as the section location moves downstream. Because of the inflection point of the mean velocity profile, numerical truncation errors trigger the transition of the boundary layer. This type of mean velocity profile is sufficiently unstable to force the flow transition without introducing artificial perturbations. Fig. 7a shows that these oscillations, essentially composed of the frequency $f = 90{,}000$ Hz, appear in the LSB and quickly grow when convected along the bubble until non-linear effects lead to a large bandwidth spectrum.

### 5.3. Stability analysis of the mean flow

To ensure that the computation with the M2 grid gives a physical description of the transition, we have achieved a local linear stability analysis [19]. The LES mean velocity profile in the LSB is considered as basic flow and the flow

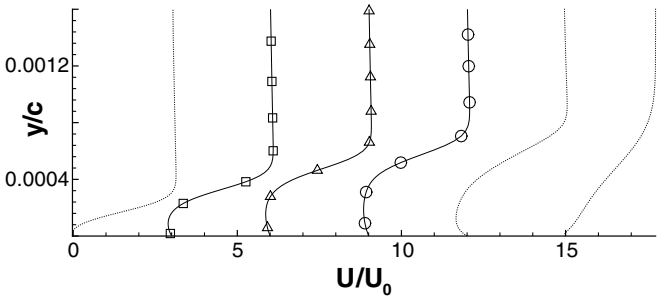


Fig. 6. Mean velocity profiles in local frame at six stages in the LSB (LES M2).

solution variables are expressed as a superposition of the basic flow and the disturbances quantities. Then, linearizing the Navier–Stokes system and using normal modes, we obtain the Orr–Sommerfeld equation. To solve numerically this eigenvalue problem, a Chebyshev collocation method is used. Then, we have performed both temporal and spatial analyses for different mean velocity profiles in the LSB. Let us notice that the basic flow is assumed to be parallel, whereas the mean velocity profile strongly changes in the LSB (see Fig. 6). Nevertheless, the LSB is elongated enough to consider the flow locally parallel ($\lambda/L_b \simeq 1/8$, where $\lambda$ is the wavelength and $L_b$ is the bubble length).

A spatial analysis has been performed for different mean velocity profiles represented in Fig. 6. For this type of analysis, the wave length $\lambda$ and the spatial growth rate $\alpha_i$ of the disturbance are computed for different values of the frequency $f$. The results show that a positive spatial growth rate is found for a frequency range, which proves, as expected, that the inflectional mean velocity profile in the LSB is highly unstable (see Fig. 7b). Increasing the value of the Reynolds number in the Orr–Sommerfeld equation leads the same results, which indicates that this disturbance results from a Kelvin–Helmholtz instability mechanism. Furthermore, the value of the most unstable frequency is about 90,000 Hz, which is in good agreement with the value obtained numerically with the M2 grid.

Then, considering the flow as weakly non-parallel, the spatial evolution of the most unstable disturbance can be calculated, thanks to the values of the local spatial growth rate obtained for each mean flow. As can be seen in Fig. 8a, the LES results are not far from the linear stability theory. The discrepancy between the two spatial growth rates is about 25%, which is acceptable considering the assumptions of this analysis. The lower value of the LES growth rate may be explained by the numerical dissipation and by the interaction of this 2D mode with 3D structures which they coexist with.

To complete this analysis, the theoretical eigenmode shape is compared to the numerical results. The LES profile of the most unstable mode is obtained by considering the amplitude of the constant frequency $f = 90{,}000$ Hz in the Fourier transforms of the velocity at several distances to the wall. Fig. 8b shows a good agreement of the location of the eigenmode shape peak (corresponding to a displacement thickness of $\delta_1 \approx 1$). However, one can see that the

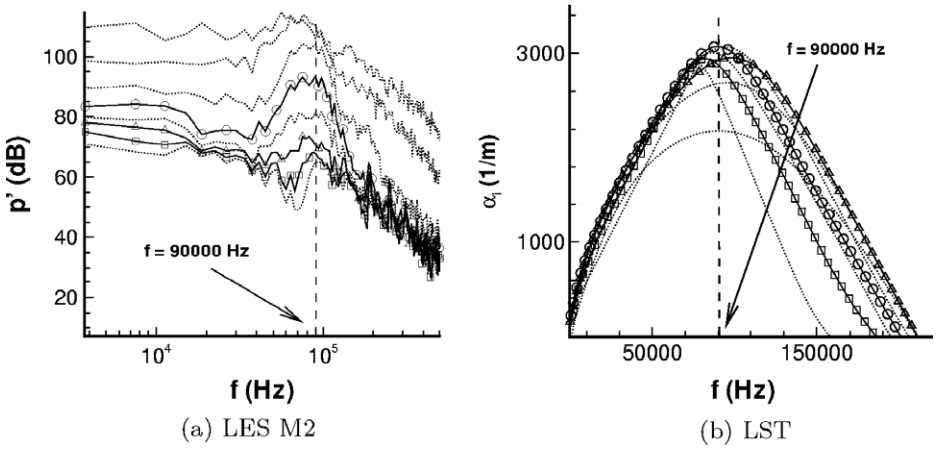


Fig. 7. Pressure spectra at different locations in the LSB (a); spatial growth rate of the disturbance $\alpha_i$ as a function of its frequency $f$ at different locations in the LSB (b).

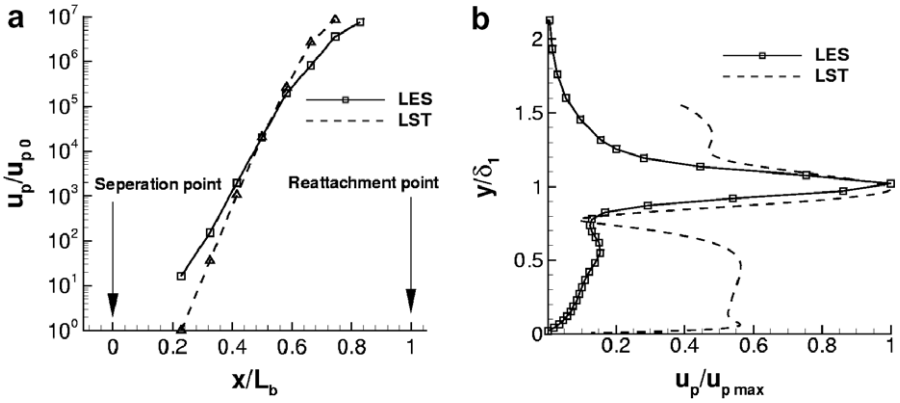


Fig. 8. Amplification of the most unstable mode $u_p/u_{p0}$ (a); Most unstable eigenmode shape in the LSB (b).

two curves do not match in the near-wall region. This discrepancy may be due to the weakly non-parallel assumption of flow considered to achieve the linear stability analysis. Indeed, the turbulent flow, at the reattachment point, may introduce large frequency range disturbances into the reverse flow of the LSB close to the wall. These disturbances interact with the main mode and alter its shape. This effect has not been taken into account in the linear stability theory, which might explain this discrepancy.

## 6. RANS/LES coupling simulation

The analysis of the results, in Section 3, seems to enlighten the deep influence of the LSB upon the downstream turbulent boundary layer, and thus, upon the simulated aerodynamics performances of the airfoil. We have shown, in Section 4, the ability of the LES tool to account for the instability mechanism that leads to the transition and the reattachment of the boundary layer. Therefore, to decrease the computation cost of the simulation, while keeping the physical mechanism of transition, a hybrid RANS/LES simulation is performed in this section. The LES domain has been reduced to the transitional zone near the leading edge, as shown in Fig. 9. The size of the LES domain is about 3 lengths of the LSB. The grid resolution, the wall normal size and the spanwise size of the LES domain are identical to those of the M2 grid. It is composed by $350 \times 65 \times 80$ grid points, respectively in the streamwise, wall normal and spanwise directions. After enough iterations to allow the flow to establish itself, statistical variables are computed in the LES domain.

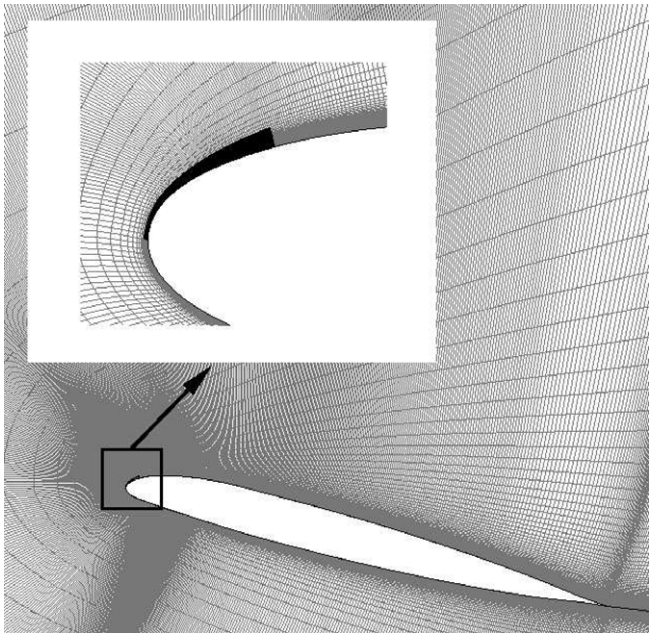

Fig. 9. RANS (grey) and LES (black) domains in the coupling simulation.

The skin friction distribution in the transitional zone obtained with this RANS/LES coupling simulation is compared to the M2 reference LES solution in Fig. 10 (left). The flow separates at the same location while the bubble length is reduced by 5% of the LES value. The Fourier analysis of the signals in the transitional zone has shown that both the frequency of the most amplified disturbance (see Fig. 11 (left)) and its spatial growth rate (see Fig. 11 (right)) are very close to the LES solution. However, its initial amplitude being higher explains the reduction of the LSB length.

Compared to the RANS fully turbulent solution, this coupling simulation enable to take into account the transition. Despite its small size, the LES domain has important consequences on the whole turbulent boundary layer calculated downstream in the RANS domain, in particular at the trailing edge where the turbulent flow separates. As shown in Fig. 10 (right), simulating the transition, with a LES domain at the leading edge, increases the turbulent separation length at the trailing edge from 12% to 16% of chord. This larger turbulent separation leads to a lower value of the lift coefficient and a greater value of the drag coefficient than the full RANS values, as shown in Table 4. The RANS/LES results are, however, different from the LES results. Indeed, the flow aims at reaching the full RANS solution, as indicated by the discontinuity of $C_f$ (see Fig. 10 (left)). A part of the information seems to be lost

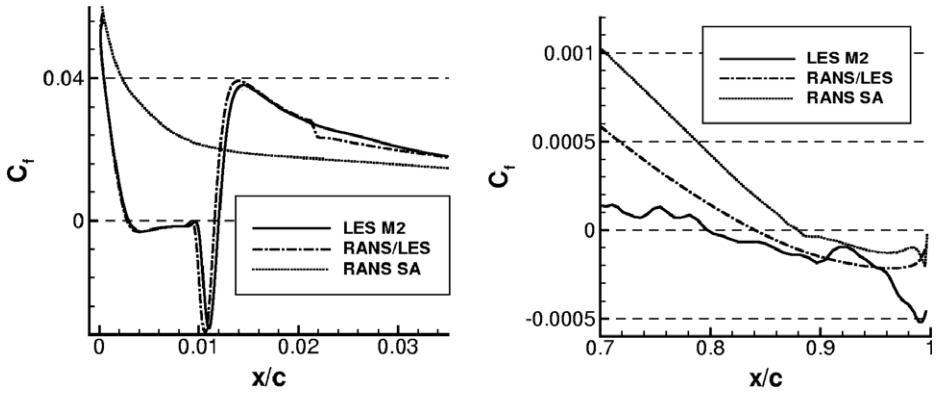


Fig. 10. Skin friction coefficients at the leading edge (left) and at the trailing edge (right).

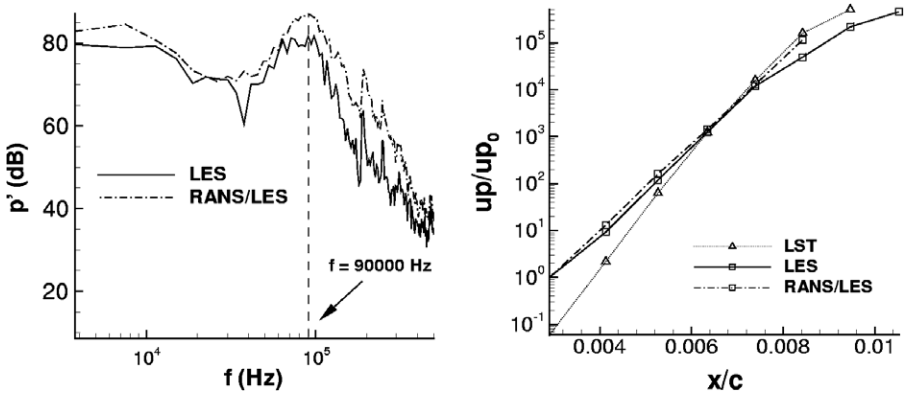


Fig. 11. LES and RANS/LES pressure spectra in the LSB (left) and spatial evolution of the most unstable mode (right).

Table 4
Experimental and numerical lift and drag coefficients

| | Experiment | LES M2 | RANS SA | RANS/LES |
|---|---|---|---|---|
| Lift | 1.416 | 1.366 | 1.487 | 1.429 |
| Drag | 0.029 | 0.039 | 0.023 | 0.033 |

where convected in the RANS domain. Some improvements are underway [3]. Nevertheless, this first RANS/LES coupling simulation is very encouraging, and it emphasizes the transition effect on the whole downstream flow and thereby on the aerodynamic characteristics of the airfoil.

## 7. Conclusion

LES of the flow around an airfoil profile at high angle of attack has been achieved. A grid refinement study has been performed and the analysis of the results underlines the strong effect of the LSB structure on the whole downstream flow and, in particular, on the length of the turbulent separation at the trailing edge. The transition mechanism in the LSB of the LES obtained with the finer grid has been compared to a linear stability analysis, and a good agreement has been observed. This shows that the computed transition seems to result from a Kelvin–Helmholtz inviscid instability mechanism. Then, a RANS/LES coupling method with a LES domain located in the transitional area has been employed for the same flow configuration. A good agreement with the LES has been obtained in the transitional and separated flow. Therefore, it seems that a reduced LES domain does not affect the transition mechanism. The results of this simulation, compared to a full RANS simulation, show the improvement of the solution thanks to a more physical description of the transitional and separated flow. However, the Spalart–Allmaras model does not seem the best adapted to convect downstream the information coming from LES. Hence, different turbulence models, specially two-equations models, will be used in the RANS domain, to study their behaviors in the RANS/LES coupling framework.

## Acknowledgements

The authors acknowledge the ONERA staff. We thank, in particular, Michel Costes, from the Applied Aerodynamics Department, for his advices and his knowledge concerning stall phenomenon. We would like to thank Daniel Arnal and Grégoire Casalis, from Aerodynamics Modeling Department, for enlightening discussions about instability mechanisms. We wish to thank Guillaume Desquesnes, from CFD Department, who has been helpful in the development of the stability analysis code. Finally, I would like to thank Mathieu Kendrick for the language corrections of this manuscript.

## References

[1] Szydlowski J, Costes M. Simulation of flow around a static and oscillating in pitch NACA0015 airfoil using URANS and DES. In: ASME transfer/fluids engineering summer conference, July Charlotte, US; 2004.
[2] Gleize V, Szydlowski J, Costes M. Numerical and physical analysis of turbulent viscous flow around a NACA0015 profile at stall. In: European congress on computational methods in applied sciences and engineering, Jyväskylä, Finland; 2004.
[3] Nolin G, Mary I, Ta-Phuoc L. RANS eddy viscosity reconstruction from LES flow field for turbulent boundary layers. AIAA Paper 2005-0143, Toronto, Canada, 2005.
[4] Sagaut P, Deck S, Terracol T. Multiscale and multiresolution approaches in turbulence. Imperial College Press; 2006.
[5] Lenormand E, Sagaut P, Ta Phuoc L, Comte P. Subgrid-scale models for large-eddy simulations of compressible wall bounded flows. AIAA J 2000;38(8):1340–50.
[6] Mary I, Nolin G. Zonal grid refinement for large eddy simulation of turbulent boundary layers. AIAA Paper 2004-0257. Reno, US, 2004.
[7] Mary I, Sagaut P. LES of a flow around an airfoil near stall. AIAA J 2002;40(6):1139–45.
[8] Larchevêque L, Sagaut P, Mary I, Labbé O, Comte P. Large-eddy simulation of a compressible flow past a deep cavity. Phys Fluids 2003;15(1):193–210.
[9] Raverdy B, Mary I, Sagaut P, Liamis L. High-resolution large-eddy simulation of the flow around a low pressure turbine blade. AIAA J 2003;41(3):390–7.
[10] Pailhas G, Houdeville R, Barricau P, Le Pape A, Faubert A, Loiret P, et al. Experimental investigation of dynamic stall. In: 31th european rotorcraft forum, September Florence, Italy; 2005.

[11] Zang T. Numerical simulation of the dynamics of turbulent boundary layers: perspectives of a transition simulator. Philos Trans Royal Soc Lond A 1991;336:95–102.
[12] Zahrai S, Bark FH, Karlsson RI. On anisotropic subgrid modeling. Eur J Mech B/Fluid 2003;14(4):459–86.
[13] Roberts WB. Calculation of laminar separation bubbles and their effect on airfoil performance. AIAA J 1980;18(1):25–30.
[14] Mack LM. Transition prediction and linear stability theory. AGARD CP-224, 1977, p. 1-1–1-22.
[15] Yorke CP, Coleman GN. Assessment of common turbulence models for an idealised adverse pressure gradient flow. Eur J Mech B/Fluids 2004;23:319–37.
[16] Aubertine CD, Eaton JK. Turbulence development in a non-equilibrium turbulent boundary layer with mild adverse pressure gradient. J Fluid Mech 2005;532:345–64.
[17] Coleman GN, Kim J, Spalart P. Direct numerical simulation of a decelerated wall-bounded turbulent shear flow. J Fluid Mech 2003;495:1–18.
[18] Spalart P, Watmuff JH. Experimental and numerical study of a turbulent boundary layer with pressure gradients. J Fluid Mech 1993;249:337–71.
[19] Schmid PJ, Henningson DS. Stability and transition in shear flows. Springer-Verlag; 2001.
[20] Yang Z, Voke PR. Large-eddy simulation of boundary-layer separation and transition at a change of surface curvature. J Fluid Mech 2001;439:305–33.
[21] Augustin K, Rist U, Wagner S. Investigation of 2D and 3D boundary-layer disturbances for active control of laminar separation bubbles. AIAA Paper 2003-613 Reno, US, 2003.